Available online at www.sciencedirect.com
ScienceDirect
Journal of Computational Physics 221 (2007) 63–87
JOURNAL OF COMPUTATIONAL PHYSICS
www.elsevier.com/locate/jcp

# A low numerical dissipation patch-based adaptive mesh refinement method for large-eddy simulation of compressible flows

C. Pantano [a,*], R. Deiterding [b], D.J. Hill [a], D.I. Pullin [a]

[a] *Graduate Aeronautical Laboratories, California Institute of Technology, 1200 E. California Blvd., Pasadena, CA 91125, United States*
[b] *Applied and Computational Mathematics, California Institute of Technology, 1200 E. California Blvd., Pasadena, CA 91125, United States*

Received 30 August 2005; received in revised form 13 April 2006; accepted 3 June 2006
Available online 26 July 2006

**Abstract**

We present a methodology for the large-eddy simulation of compressible flows with a low-numerical dissipation scheme and structured adaptive mesh refinement (SAMR). A description of a conservative, flux-based hybrid numerical method that uses both centered finite-difference and a weighted essentially non-oscillatory (WENO) scheme is given, encompassing the cases of scheme alternation and internal mesh interfaces resulting from SAMR. In this method, the centered scheme is used in turbulent flow regions while WENO is employed to capture shocks. One-, two- and three-dimensional numerical experiments and example simulations are presented including homogeneous shock-free turbulence, a turbulent jet and the strongly shock-driven mixing of a Richtmyer–Meshkov instability.


*Keywords:* SAMR; LES; Numerical methods; Compressible flow; Turbulence

## 1. Introduction

Compressible flows of practical interest generally involve a number of physically different key features. In some regions, the level of compressibility may be sufficiently high to form shock waves. In other locations, the flow may be turbulent, and yet in other regions both shocks and turbulence may coexist. Practical numerical simulation of these flows often necessitates a certain degree of dynamic resolution adaptation. For the Euler equations, structured adaptive mesh refinement (SAMR) [1,2] is particularly efficient as it effectively allows for both temporal and spatial mesh adaptation. Additionally, the adequate numerical treatment of inherently different flow features is often best accomplished by using different numerical methods based on local criteria, for example, switched or hybrid methods that change the numerical stencil around shocks and revert to centered stencils in smooth regions [3–7]. Centered finite-difference methods have been used with explicit artificial

* Corresponding author. Tel.: +1 626 395 8534.
*E-mail address:* cpantano@galcit.caltech.edu (C. Pantano).

0021-9991/$ - see front matter 
doi:10.1016/j.jcp.2006.06.011

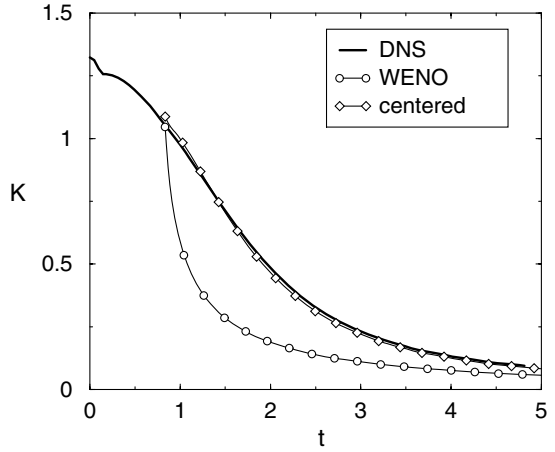


Fig. 1. Comparison of decay of turbulence kinetic energy in a homogeneous decaying compressible LES computed on a grid of $32^3$ points using WENO vs. centered scheme. DNS computed with a $256^3$ grid and a padé method.

viscosity to regularize shocks in non-conservative form [8], and as a penalty based finite-difference method [9] for shockless flows. Other hybrid methods include [10], where transport property models change depending on local flow conditions. In general, scheme alternation has often been found to be appropriate when high fidelity solutions are to be obtained at minimal computational expense.

As front tracking is extremely difficult in three-dimensional flows and shock waves cannot be fully resolved (the shock thickness is of the order of the mean free path), numerical methods for compressible flows usually try to capture shock waves and their interactions on an under-resolved mesh. According to the Lax–Wendroff theorem [11], the convergence of shock-capturing methods toward a weak solution of the Euler equations requires the discrete conservation of mass, momentum and energy. In SAMR methods, this property is typically accomplished by using flux-based finite volume discretizations (see for instance [12] for a general introduction), although non-flux-based formulations are also possible [13]. Flux-based extensions of the Berger–Colella SAMR method, originally developed for time-explicit finite volume schemes, to time-implicit problems which include combustion [14] and radiation [15,16], are also available.

Apart from conservation, differing flow features may demand different numerical approaches. For example, shocks and contact discontinuities are typically smoothed over the available grid points by performing some form of controlled upwind-biased differentiation of the fluxes (that we will refer to as upwinding from this point), but flows involving turbulence require a different strategy since the complicated flow structure demands a more accurate spectral representation. For turbulence in the high Reynolds number regime, large-eddy simulation (LES) is a practical approach in which only the large scales of the flow are simulated directly and the small scales are modeled. Turbulent flows are usually of a wavy nature, and upwinding techniques introduce substantial numerical dissipation that tends to artificially remove energy from the highest resolved wavenumbers. In order to avoid interference with the flow physics, transport schemes suitable for LES therefore have to represent the energy transfer between wavelengths as accurately as possible [17]. Experience in LES with explicitly modeled subgrid terms has shown that it is best to use numerical methods with minimal numerical dissipation for the resolved-scale flow. Such schemes can be constructed by the use of centered numerical stencils but care must be taken to avoid non-linear instabilities as there is no intrinsic numerical stabilization. This can be achieved to some extent by using kinetic energy conserving (skew-symmetric) formulations [18–21]. Fig. 1 demonstrates the efficacy of LES when using an appropriate numerical method. It compares the decay of turbulence kinetic energy between a direct numerical simulation (DNS) [22][1] and LES with either the 5-point centered-difference scheme outlined in this paper or the standard shock-capturing scheme WENO-5. Although the WENO scheme has the same stencil width as the centered method, the inherit numerical dis-

[1] Case D9 with microscale Reynolds number of 175 and turbulent Mach number of 0.488 at $256^3$ resolution.

sipation of a shock-capturing scheme produces an unsuitable result for this canonical turbulent flow of homogeneous decaying compressible turbulence.

Just as LES can make the simulation of certain turbulent flows numerically tractable by focusing on the scales of interest, SAMR can provide large computational savings when important localized flow features have higher resolution requirements then the majority of the flow. In traditional applications, such features include shocks, contacts, and other regions such as induction zones in detonations. The importance of resolution adaptation for LES has recently been highlighted [23]. In our treatment of LES with SAMR, we recognize that, in addition to the previously mentioned features, turbulent regions in a flow also have their own resolution requirements. For example, large computational savings can be achieved when the turbulent regions of the flow do not fill the entire flow domain as will be seen in the simulations presented in Section 6.

In this paper, we present a dynamically-adaptive, three-dimensional hybrid finite-difference method that is conservative and has low numerical dissipation. To obtain the computational efficiency of SAMR, we extend the Berger and Colella [2] algorithm to accommodate the requirements of hybrid shock dynamics/large-eddy simulations with such a numerical method. In general, many of the difficulties that are encountered in low dissipation methods with SAMR are related to stability issues that arise at interfaces between meshes of different spacing [24]. A successful approach to stabilize the simulations is to filter the fluid mechanical fields with low-pass filters tuned to minimize their effect on the large flow scales [25]. In practice this is just a more sophisticated form of global numerical dissipation that we wish to avoid. In our approach any such dissipation is physically isolated to the coarse-fine boundaries and is best described within the numerical scheme. Our hybrid numerical method has two components: a finite-difference WENO scheme [26,4] to be used around discontinuities (both physical and due to mesh resolution changes) and a conservative, tuned centered-difference (TCD) scheme (but in skew-symmetric form) in the smooth or turbulent regions of the flow. The WENO and centered-difference methods are specially tuned to minimize dispersive errors at those locations where scheme switching takes place. The present work is the evolution of [7] to SAMR meshes. The principal advantage of finite-difference formulations of the WENO method, as opposed to finite volume, is largely related to efficiency (especially in three-dimensions); the multi-dimensional reconstruction step of the finite volume version can be avoided completely and no multi-point quadrature rule has to be used in the numerical flux approximation.

The outline of the paper follows a prescription from the general to the specific, from framework of the SAMR for hyperbolic systems, through the equations of motion and the numerical method to simulations. Section 2 describes the SAMR formulation with particular attention paid to the complications owing to the requirements of LES. The following sections describe the LES equations of motion (Section 3) and their implementation in this framework by means of the flux-based low dissipation numerical method (Section 4). Section 5 investigates convergence and numerical dissipation. Finally, Section 6 presents three-dimensional examples of LES simulations and comparisons with experiments. Appendix A discusses the choice of boundary stencils and boundary conditions and Appendix B discusses the subgrid closure.

## 2. Structured adaptive mesh refinement

The SAMR method after Berger and Colella [2] is a dynamic mesh adaptation technique for hyperbolic systems tailored for time-explicit finite volume schemes on block-structured Cartesian meshes. Such schemes are typically derived from a conservation law

$$\frac{\partial \boldsymbol{q}}{\partial t} + \frac{\partial}{\partial x_k}\boldsymbol{f}^k(\boldsymbol{q}) = 0, \tag{1}$$

where $\boldsymbol{q}$ is the vector of state and $\boldsymbol{f}^k$ denotes the flux vector, utilizing a cell-wise update formula of the general form

$$\boldsymbol{Q}^{n+1} = \boldsymbol{Q}^n - \frac{\Delta t}{\Delta x_k}\Delta \boldsymbol{F}^k(\boldsymbol{Q}^n). \tag{2}$$

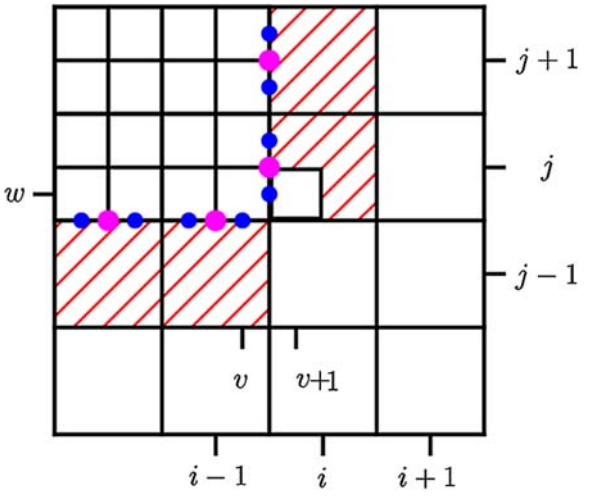


Fig. 2. Location of numerical fluxes required for flux correction. Cells to correct are shaded.

Herein, $\Delta \boldsymbol{F}^k(\boldsymbol{Q}^n)/\Delta x_k$ denotes the difference quotient of the numerical flux function in the $k$th spatial direction that locally approximates the derivative of the flux vector $\boldsymbol{f}^k$. The discrete analogue of the conservative variable vector $\boldsymbol{q}$ at time $t = n\Delta t$ is denoted by $\boldsymbol{Q}^n$, where, for simplicity, we have omitted all spatial indices.[2]

Characteristic for the idea of structured mesh adaptivity is that Eq. (2) is technically not implemented in a cell-based fashion but rather in a routine which operates on equidistant subgrids which become computationally decoupled during one update through the use of ghost or halo cells. This enables an increased computational performance, but requires a subsequent correction operation at coarse-fine boundaries to construct a combined numerical solution on the non-uniform mesh.

### 2.1. SAMR integration cycle

SAMR uses a hierarchy of successively embedded level domains that are recursively constructed by grouping cells tagged for refinement into non-overlapping rectangular grids. All spatial All spatial mesh widths $\Delta x_k$ and the temporal resolution $\Delta t$ are set to be $r_l$-times finer on level $l$ than on level $l-1$, i.e., $\Delta t_l := \Delta t_{l-1}/r_l$ and $\Delta x_{k,l} := \Delta x_{k,l-1}/r_l$ with $r_l \in \mathbb{N}, r_l \geqslant 2$ for $0 < l \leqslant l_{\max}$ and $r_0 = 1$, and time-explicit schemes of the form (2) in principle remain stable on all levels of the hierarchy.

Different levels are integrated recursively in time allowing the derivation of interpolated boundary conditions of Dirichlet-type from the coarser level at coarse-fine interfaces. In this paper, we utilize a linear interpolation in time, cf. [2], and a locally conservative linear interpolation operation in space that is detailed in Section 2.2. When a fine level $l+1$ reaches the same discrete time as the next coarser level $l$, values of cells covered by finer subgrids are overwritten by averaged fine grid values. This averaging or *restriction* operation enhances the approximation on the coarser grid and synchronizes both levels. The restriction leads to a violation of the discrete conservation property on the coarse level as it neglects numerical fluxes between the fine and the coarse-level domains. In order to ensure a conservative coarse-fine boundary matching, the coarse-flux approximation adjacent to modified coarse-level cells is replaced with the sum of all overlying fine level fluxes, cf. [2]. For simplicity, but also for accuracy of the approximation, we require that the hierarchy is *properly nested*, which means that only cells of level $l$ need to be corrected with accumulated level $l+1$ fluxes. As an example, we sketch this operation in two space dimensions for cell $(i,j)$ in Fig. 2. After the update on level $l$ the correction term $\delta \boldsymbol{F}^{1,l+1}_{i-\frac{1}{2},j}$ is initialized by $\delta \boldsymbol{F}^{1,l+1}_{i-\frac{1}{2},j} := -\boldsymbol{F}^{1,l}_{i-\frac{1}{2},j}$. During the $r_{l+1}$ update steps of level $l+1$ all necessary fine level fluxes are accumulated, i.e.

[2] Note that throughout the text we use bold notation to denote vector quantities and employ the convention that repeated indices imply summation unless stated otherwise.

$$\delta \boldsymbol{F}^{1,l+1}_{i-\frac{1}{2},j} := \delta \boldsymbol{F}^{1,l+1}_{i-\frac{1}{2},j} + \frac{1}{r^2_{l+1}} \sum_{m=0}^{r_{l+1}-1} \boldsymbol{F}^{1,l+1}_{v+\frac{1}{2},w+m}(t + \kappa \Delta t_{l+1}). \tag{3}$$

When the integration of the fine level is complete, the correction is applied by calculating $\boldsymbol{Q}^{n+1}_{ij} := \boldsymbol{Q}^{n+1}_{ij} + \frac{\Delta t_l}{\Delta x_{1,l}} \delta \boldsymbol{F}^{1,l+1}_{i-\frac{1}{2},j}$.

### 2.2. SAMR prolongation operator

A crucial operation in SAMR is the interpolation or *prolongation* operator that is necessary to transfer data from coarser meshes into refined meshes. The original sources on SAMR [1,2] suggest the use of a bi-linear spatial interpolation operation that preserves the monotonicity of the solution, but satisfies only a discrete conservation property in the global sense. While this choice is unproblematic for typical shock wave problems, it is inappropriate for large-eddy simulations given the little amount of numerical stabilization that a centered differencing provides throughout the entire SAMR hierarchy (see also Section 4.1). All simulations throughout this paper were therefore done with locally conservative linear operations. For the exemplary fine cell $(v+1, w)$ in Fig. 2 the prolongation operator employed reads

$$\boldsymbol{Q}^{l}_{v+1,w} := \boldsymbol{Q}^{l-1}_{ij} + v_1(\boldsymbol{Q}^{l-1}_{i+1,j} - \boldsymbol{Q}^{l-1}_{i-1,j}) + v_2(\boldsymbol{Q}^{l-1}_{i,j+1} - \boldsymbol{Q}^{l-1}_{i,j-1}) \tag{4}$$

with factors $v_1 = v_2 = -1/8$. As we use a refinement strategy carefully tailored for our problem class, cf. Section 5, the lack of monotonicity preservation of Eq. (4) does not cause any problems in our simulations.

### 2.3. Runge–Kutta scheme for SAMR

Our use of a centered (non-dissipative) scheme imposes additional restrictions on the time integration method. We are interested here in explicit multi-stage schemes for ease of implementation within SAMR. Owing to the stability properties of these explicit integration schemes, the preferred practical self-starting methods with the ability of inexpensive time adaptation in SAMR are Runge–Kutta-type methods of third or higher order. Lower-order Runge–Kutta methods are not stable for purely convective problems, the dominant character of the LES equations at high Reynolds numbers. Moreover, the use of upwinding in WENO imposes additional temporal stability restrictions at discontinuities. These stability restrictions are associated with the WENO operator and lead to undesired oscillations at shocks if the coefficients of the Runge–Kutta method are not all positive (substages of the scheme can be unstable). For these reasons, we use the optimal third-order strong stability preserving (SSP) Runge–Kutta scheme of [29] that posses the total variation diminishing (TVD) property provided the single-step operator of Eq. (2) is TVD. Time advancement is accomplished following

$$\tilde{\boldsymbol{Q}}^{\upsilon} = \alpha_\upsilon \boldsymbol{Q}^n + \beta_\upsilon \tilde{\boldsymbol{Q}}^{\upsilon-1} + \gamma_\upsilon \frac{\Delta t}{\Delta x_k} \Delta \boldsymbol{F}^k(\tilde{\boldsymbol{Q}}^{\upsilon-1}), \tag{5}$$

successively for $\upsilon = 1, \ldots, \Upsilon$. The coefficients $\alpha_\upsilon$, $\beta_\upsilon$ and $\gamma_\upsilon$ are given in [29] and take the values shown in Table 1. The iteration is started with $\tilde{\boldsymbol{Q}}^0 := \boldsymbol{Q}^n$ and $\alpha_1 = 1$, $\beta_1 = 0$. After the final stage $\Upsilon$ the next time step is given by $\boldsymbol{Q}^{n+1} := \tilde{\boldsymbol{Q}}^{\Upsilon}$. The entire iteration can be implemented storage-efficiently by updating only $\boldsymbol{Q}^{n+1}$. Applying Eq. (5) successively yields the expression

$$\boldsymbol{Q}^{n+1} = \boldsymbol{Q}^n - \sum_{\upsilon=1}^{\Upsilon} \varphi_\upsilon \frac{\Delta t}{\Delta x_k} \Delta \boldsymbol{F}^k(\tilde{\boldsymbol{Q}}^{\upsilon-1}) \quad \text{with} \quad \varphi_\upsilon = \gamma_\upsilon \prod_{\nu=\upsilon+1}^{\Upsilon} \beta_\nu \tag{6}$$

Table 1
Coefficients of the optimal 3rd order SSP Runge–Kutta scheme of [29] and the flux-correction coefficient $\varphi_\upsilon$

| $\upsilon$ | $\alpha_\upsilon$ | $\beta_\upsilon$ | $\gamma_\upsilon$ | $\varphi_\upsilon$ |
|---|---|---|---|---|
| 1 | 1 | 0 | 1 | $\frac{1}{6}$ |
| 2 | $\frac{3}{4}$ | $\frac{1}{4}$ | $\frac{1}{4}$ | $\frac{1}{6}$ |
| 3 | $\frac{1}{2}$ | $\frac{2}{3}$ | $\frac{2}{3}$ | $\frac{2}{3}$ |

as conservative update formula for a multi-stage method instead of Eq. (2). The effective flux pre-factors $\varphi_\upsilon$ are essential to implement the SAMR flux correction. The computation of the previous correction term in Eq. (3) is then realized as

$$\delta \boldsymbol{F}^{1,l+1}_{i-\frac{1}{2},j} := -\varphi_1 \boldsymbol{F}^{1,l}_{i-\frac{1}{2},j}(\tilde{\boldsymbol{Q}}^0), \quad \delta \boldsymbol{F}^{1,l+1}_{i-\frac{1}{2},j} := \delta \boldsymbol{F}^{1,l+1}_{i-\frac{1}{2},j} - \sum_{\upsilon=2}^{\Upsilon} \varphi_\upsilon \boldsymbol{F}^{1,l}_{i-\frac{1}{2},j}(\tilde{\boldsymbol{Q}}^{\upsilon-1}), \tag{7}$$

on level $l$ and

$$\delta \boldsymbol{F}^{1,l+1}_{i-\frac{1}{2},j} := \delta \boldsymbol{F}^{1,l+1}_{i-\frac{1}{2},j} + \frac{1}{r^2_{l+1}} \sum_{m=0}^{r_{l+1}-1} \sum_{\upsilon=1}^{\Upsilon} \varphi_\upsilon \boldsymbol{F}^{1,l+1}_{\upsilon+\frac{1}{2},w+m}(\tilde{\boldsymbol{Q}}^{\upsilon-1}(t+\kappa\Delta t_{l+1})), \tag{8}$$

on level $l+1$. For all simulations throughout this paper we have employed this algorithm together with the optimal third-order SSP Runge–Kutta scheme of [29], but we note that it is equally applicable to other explicit Runge–Kutta schemes. For instance, the coefficients $\alpha_{1,\ldots,3} = 1$, $\beta_{1,\ldots,3} = 0$, $\gamma_1 = \frac{1}{3}$, $\gamma_2 = \frac{1}{2}$, $\gamma_3 = 1$ correspond to a standard three-stage scheme.

## 3. Governing equations

The governing equations of LES of compressible flows are formulated using Favre-filtered variables, defined for an arbitrary function of Cartesian space, $\boldsymbol{x}$ and time, $t$ and denoted by $\phi(\boldsymbol{x}, t)$ as

$$\tilde{\phi} = \frac{\overline{\rho\phi}}{\bar{\rho}}, \tag{9}$$

where $\rho$ is the density and the overbar denotes the "conceptual" filter operator, defined by

$$\bar{\phi}(\boldsymbol{x}, t; \Delta_c) = \int G(\boldsymbol{x} - \boldsymbol{x}'; \Delta_c)\phi(\boldsymbol{x}', t)\,\mathrm{d}\boldsymbol{x}', \tag{10}$$

with $G(\boldsymbol{x} - \boldsymbol{x}';\Delta_c)$ representing the filter kernel with compact support and $\Delta_c$ the subgrid cutoff length scale. The idea behind LES is that one computes the temporal evolution of $\bar{\phi}(\boldsymbol{x}, t; \Delta_c)$ or $\tilde{\phi}(\boldsymbol{x}, t; \Delta_c)$ while all scales below $\Delta_c$ are not resolved but modeled by a subgrid closure. We remark that this filtering operation is never explicitly performed in an actual LES calculation. We, therefore, view this primary filtering as a conceptual device that connects the Navier–Stokes equations to the LES model equations. It is introduced here for completeness. In what follows, for clarity, we will drop the explicit dependence on $\Delta_c$.

Conservation of mass, momentum, energy and $M$ species mass fractions are expressed by the corresponding filtered transport equations. Presented in the form of Eq. (1) the conservative vector of state becomes

$$\boldsymbol{q} = (\bar{\rho}, \bar{\rho}\tilde{u}_1, \bar{\rho}\tilde{u}_1, \bar{\rho}\tilde{u}_3, \overline{E}, \bar{\rho}\widetilde{Y}_1, \ldots, \bar{\rho}\widetilde{Y}_M)^{\mathrm{T}}, \tag{11}$$

while the total directional flux vectors are decomposed for clarity,

$$\boldsymbol{f}^k(\boldsymbol{q}) = \boldsymbol{f}^k_{\mathrm{inv}}(\boldsymbol{q}) + \boldsymbol{f}^k_{\mathrm{vis}}(\boldsymbol{q}) + \boldsymbol{f}^k_{\mathrm{sgs}}(\boldsymbol{q}), \tag{12}$$

into the inviscid fluxes, the resolved-scale viscous fluxes and the subgrid scale terms which represent unresolved stresses and other transfers between the resolved scales and the subgrid. Mathematically these are given by

$$\boldsymbol{f}^k_{\mathrm{inv}}(\boldsymbol{q}) = \begin{pmatrix} \bar{\rho}\tilde{u}_k \\ \bar{\rho}\tilde{u}_1\tilde{u}_k + \delta_{1k}\bar{p} \\ \bar{\rho}\tilde{u}_2\tilde{u}_k + \delta_{2k}\bar{p} \\ \bar{\rho}\tilde{u}_3\tilde{u}_k + \delta_{3k}\bar{p} \\ (\overline{E} + \bar{p})\tilde{u}_k \\ \bar{\rho}\widetilde{Y}_1\tilde{u}_k \\ \vdots \\ \bar{\rho}\widetilde{Y}_M\tilde{u}_k \end{pmatrix}, \quad \boldsymbol{f}^k_{\mathrm{vis}}(\boldsymbol{q}) = \begin{pmatrix} 0 \\ -\tilde{\sigma}_{1k} \\ -\tilde{\sigma}_{2k} \\ -\tilde{\sigma}_{3k} \\ \tilde{q}_k - \tilde{\sigma}_{kj}\tilde{u}_j \\ \tilde{J}^1_k \\ \vdots \\ \tilde{J}^M_k \end{pmatrix}, \quad \boldsymbol{f}^k_{\mathrm{sgs}}(\boldsymbol{q}) = \begin{pmatrix} 0 \\ \tau_{1k} \\ \tau_{2k} \\ \tau_{3k} \\ \sigma^e_k \\ \sigma^1_k \\ \vdots \\ \sigma^M_k \end{pmatrix}. \tag{13}$$

The resolved fields are denoted by $\bar{\rho}$ for density, $\tilde{u}_k$ for the velocity components, $\bar{p}$ for pressure, $\overline{E}$ for total energy and $\widetilde{T}$ for temperature. The resolved deviatoric Newtonian viscous stress tensor is defined as

$$\tilde{\sigma}_{ik} = \tilde{\mu}\left(\frac{\partial \tilde{u}_k}{\partial x_i} + \frac{\partial \tilde{u}_i}{\partial x_k}\right) - \frac{2}{3}\tilde{\mu}\frac{\partial \tilde{u}_j}{\partial x_j}\delta_{ik}, \tag{14}$$

and the resolved heat conduction and species diffusion terms are given by

$$\tilde{q}_k = -\tilde{\lambda}\frac{\partial \widetilde{T}}{\partial x_k} \quad \text{and} \quad \tilde{J}_k^m = -\bar{\rho}\tilde{D}_m\frac{\partial \widetilde{Y}_m}{\partial x_k}, \tag{15}$$

respectively, with no sum on the species index $m$. The resolved shear viscosity, $\tilde{\mu}$, thermal conductivity, $\tilde{\lambda}$ and species diffusivity, $\tilde{D}_m$, are typically functions of $\widetilde{T}$ and composition. In Eq. (15), heat flux contributions from enthalpy diffusion and radiation effects are neglected.

The state relationship for the total energy $\overline{E}$ includes contributions from the subgrid kinetic energy $\bar{\rho}k_{\text{sgs}}$ and subgrid enthalpy $\bar{\rho}h_{\text{sgs}}$ in the form

$$\overline{E} = \bar{\rho}h_i\widetilde{Y}_i - \bar{p} + \frac{1}{2}\bar{\rho}\tilde{u}_k\tilde{u}_k + \bar{\rho}(k_{\text{sgs}} + h_{\text{sgs}}), \tag{16}$$

where $h_i$, assumed to be a function of $\widetilde{T}$, is the enthalpy of the $i$th component of the gas mixture. The system of equations is closed thermodynamically by the equation of state

$$\bar{p} = \bar{\rho}R^{\text{o}}\widetilde{T}(\widetilde{Y}_i/W_i), \tag{17}$$

where $R^{\text{o}}$ is the universal gas constant and $W_i$ is the molecular weight of $i$th species; the subgrid contribution to the mean molecular weight due to the correlation of the mixture composition and temperature are neglected. In the numerical simulations presented in this paper, the individual enthalpies are modeled as linear functions of temperature.

The subgrid flux terms, $\boldsymbol{f}^k_{\text{sgs}}(\boldsymbol{q})$, for momentum $\tau_{ik}$, energy $\sigma^e_k$ and species $\sigma^m_k$ must be provided for full LES closure in addition to related models for the subgrid kinetic energy $k_{\text{sgs}}$ and enthalpy $h_{\text{sgs}}$. In our use of LES, we also assume that the model dependence on $\Delta_{\text{c}}$ is only parametric and that $\Delta_{\text{c}}$ is at most a slowly varying function of spatial coordinates so any subgrid contribution from this variation is negligible. The calculation of the modeling terms from the resolved-scale quantities for our simulations was based on the stretched-vortex model [30–32] and is summarized in Appendix B.

## 4. Numerical method

In this section, we focus on the discrete spacial representation of our system. Standard SAMR methodology requires a flux-based numerical scheme formulated on a Cartesian uniform grid. This method is then applied to each grid (patch) of the mesh hierarchy. The derivatives of inviscid fluxes $\boldsymbol{f}^k_{\text{inv}}$ are presently computed using a hybrid finite-difference method with a 5-point tuned centered-difference (TCD) scheme in smooth or turbulent regions of the flow and a 5-point WENO upwinded scheme [33] at discontinuities. The WENO stencil coefficients have been adjusted such that the optimal stencil matches the TCD stencil (cf. Eq. (18) below). This modification largely eliminates any dispersion errors that result when transitioning between schemes. If this is not done, a mismatch of modified wavenumber behavior results, leading to undesirable dispersion errors that are very similar in nature to those that arise in discretizations with variable spacing between co-located points described by [34]. The main difference between the formulation presented here and [7] is the reformulation in terms of the discretely more stable skew-symmetric form, which we now discuss.

### 4.1. Stable TCD formulation

Consider a one-dimensional uniform discretization of the independent coordinate $x$ with grid spacing $\Delta x$. The derivative of a function $f(x)$ evaluated at the point $x = j\Delta x$ can be approximated by the 5-point centered-difference operator $\mathscr{D}$,

$$\mathscr{D}f|_j \equiv \frac{1}{\Delta x}(\alpha(f_{j+2} - f_{j-2}) + \beta(f_{j+1} - f_{j-1})) \approx \left.\frac{\partial f}{\partial x}\right|_j, \tag{18}$$

where $f_j = f(j\Delta x)$ and $\beta = 1/2 - 2\alpha$ is required for second-order accuracy. The choice $\alpha = 0$ leads to the standard 2nd-order explicit stencil and the choice $-1/12$ leads to the standard 4th-order explicit stencil. In three-dimensional LES, it may be advantageous to optimize the stencil according to other criteria (not necessarily order of accuracy). This was done by [7], where the stencil was optimized to minimize truncation errors in LES [35] while maintaining 2nd-order accuracy. With this method, the parameter $\alpha$ takes the value $-0.197$ and the resulting stencil is referred to as the tuned center difference (TCD). The spectral transfer properties of the discretization are discussed in [7]. In the following exposition, we use the general formulation without specifying $\alpha$ to insure that the results are equally valid for the entire family of 5-point centered stencils.

The discrete numerical stability of the inviscid terms $\boldsymbol{f}^k_{\text{inv}}$ is a desirable property of centered discretizations for LES at high Reynolds number, since, in some flow regions, the viscous terms, and sometimes even the SGS terms, may provide only negligible stabilization. It is known that asymptotic stability can be achieved for incompressible flows by using kinetic energy preserving discretizations, also known as skew-symmetric [19]. A slightly adapted form of kinetic energy conservation is also required for compressible flows [20] away from shocks. Moreover, because we use centered stencils in the SAMR framework, the numerical method must be strictly stable at all mesh levels (even at the coarse under-resolved ones). This has no consequence on the final numerical solution because the under-resolved, coarse fields are ultimately discarded when applying the restriction operator, but it allows the use of a uniform algorithm throughout the entire hierarchy. Therefore, the momentum and species convective terms are computed numerically as

$$\frac{\partial(\bar{\rho}\tilde{u}_i\tilde{u}_k)}{\partial x_k} \to \frac{1}{2}\frac{\partial(\bar{\rho}\tilde{u}_i\tilde{u}_k)}{\partial x_k} + \frac{1}{2}\bar{\rho}\tilde{u}_k\frac{\partial\tilde{u}_i}{\partial x_k} + \frac{1}{2}\tilde{u}_i\frac{\partial(\bar{\rho}\tilde{u}_k)}{\partial x_k}, \tag{19}$$

$$\frac{\partial(\bar{\rho}\widetilde{Y}_i\tilde{u}_k)}{\partial x_k} \to \frac{1}{2}\frac{\partial(\bar{\rho}\widetilde{Y}_i\tilde{u}_k)}{\partial x_k} + \frac{1}{2}\bar{\rho}\tilde{u}_k\frac{\partial\widetilde{Y}_i}{\partial x_k} + \frac{1}{2}\widetilde{Y}_i\frac{\partial(\bar{\rho}\tilde{u}_k)}{\partial x_k}. \tag{20}$$

This numerical representation of the convective terms alone is not sufficient to improve stability of compressible flows owing to the exchanges between internal and kinetic energy that are not accounted in Eqs. (19) and (20), and result in the divergence of the thermodynamic fields including pressure and density by accumulation of aliasing errors. To improve robustness, we need to consider the convective term of the energy equation. Our constraint of enforcing discrete conservation of energy in the finite difference type discretization of SAMR restricts the formulations to those that can be written in flux form. Of these, the most stable is the skew-symmetric formulation that conserves internal energy variance given by Eq. (22) in [21], that reads

$$\frac{\partial((\overline{E}+\bar{p})\tilde{u}_k)}{\partial x_k} \to \frac{1}{2}\frac{\partial(\bar{\rho}\tilde{e}\tilde{u}_k)}{\partial x_k} + \frac{1}{2}\bar{\rho}\tilde{u}_k\frac{\partial\tilde{e}}{\partial x_k} + \frac{1}{2}\tilde{e}\frac{\partial(\bar{\rho}\tilde{u}_k)}{\partial x_k} + \frac{1}{2}\tilde{u}_i\frac{\partial\bar{\rho}\tilde{u}_i\tilde{u}_k}{\partial x_k} + \frac{1}{2}\bar{\rho}\tilde{u}_i\tilde{u}_k\frac{\partial\tilde{u}_i}{\partial x_k} + \bar{p}\frac{\partial\tilde{u}_k}{\partial x_k} + \tilde{u}_k\frac{\partial\bar{p}}{\partial x_k}, \tag{21}$$

where $\tilde{e} = \overline{E}/\bar{\rho} - \frac{1}{2}\tilde{u}_k^2$ is the total internal energy.

### 4.2. Flux-based formulation

In the present implementation, the SAMR approach is tailored specifically for flux-based discretizations [27,28]. For example, numerical approximations, $\boldsymbol{F}^k$, to the fluxes $\boldsymbol{f}^k$ formed at the cell faces are used to enforce conservation during timestep refinement; see Eq. (3). Additionally, only by use of a flux-based form can the scheme switching of our numerical method between WENO and TCD be achieved without loss of conservation. WENO schemes themselves are naturally flux-based formulations, but a flux-based formulation of the skew-symmetric center difference method is required. We briefly present the necessary ingredients.

We construct fluxes consistent with the general center-difference operator Eq. (18). The divergence-like flux $F^{\text{div}}_{j+1/2}$ satisfies

$$\mathscr{D}f\big|_j = \frac{F^{\text{div}}_{j+1/2} - F^{\text{div}}_{j-1/2}}{\Delta x}, \tag{22}$$

and $F^{\text{div}}_{j+1/2}$ may be interpreted as the approximate value of $f(x)$ at the cell face $x = (j+1/2)\Delta x$. This can be obtained readily and reads

$$F^{\text{div}}_{j+1/2} = \alpha(f_{j+2} + f_{j-1}) + (\alpha+\beta)(f_j + f_{j+1}). \tag{23}$$

The consistent flux-based discretization of Eqs. (19)–(21) requires a representation of the product rule derivative for $f(x) = a(x)b(x)$. We denote the sought term by $F^{\text{prod}}_{j+1/2}$ and require that

$$a\mathscr{D}b|_j + b\mathscr{D}a|_j = \frac{F^{\text{prod}}_{j+1/2} - F^{\text{prod}}_{j-1/2}}{\Delta x}, \tag{24}$$

be satisfied. The corresponding formula

$$F^{\text{prod}}_{j+1/2} = \alpha(a_{j+2}b_j + a_{j-1}b_{j+1} + a_jb_{j+2} + a_{j+1}b_{j-1}) + \beta(a_jb_{j+1} + a_{j+1}b_j), \tag{25}$$

may be verified by substitution in Eq. (24). The total non-dissipative skew-symmetric convective flux which satisfies

$$\frac{1}{2}(\mathscr{D}(ab)|_j + a\mathscr{D}b|_j + b\mathscr{D}a|_j) = \frac{F^{\text{skew}}_{j+1/2} - F^{\text{skew}}_{j-1/2}}{\Delta x}, \tag{26}$$

is then given by

$$F^{\text{skew}}_{j+1/2} = \frac{1}{2}(F^{\text{div}}_{j+1/2} + F^{\text{prod}}_{j+1/2}), \tag{27}$$

where $a$ and $b$ will be replaced by $\bar{\rho}\tilde{u}_k$, $\tilde{u}_k$, and $\widetilde{Y}_m$, depending on the transport equation being considered. A similar expression is derived for the energy equation by identifying divergence and product-like terms in Eq. (21). This flux-based approach greatly simplifies the implementation of a consistent and conservative scheme with SAMR [36]. A similar approach was followed by [37,6] for standard difference operators with a different energy equation formulation. Finally, the fluxes at the physical domain boundaries are computed consistently with the skew-symmetric formulation and the discrete boundary stencil discussed in Appendix A.

### 4.3. Flux switching criteria

We consider two kinds of discontinuities: physical and numerical. Physical discontinuities include shocks and contacts while numerical discontinuities include coarse-fine mesh interfaces that are akin to jumps in the Jacobian of the mesh. The utilization of upwind differentiation at mesh interfaces improves the quality of the solution (smoothness) while introducing minimal numerical dissipation, because the solution is smooth. In essence, this provides a mechanism that minimizes acoustic waves reflected or generated by the coarse-fine interfaces. This treatment is very similar in spirit to the underlying technique used in discontinuous Galerkin methods [38]. We have found that the best results are obtained when all fluxes of the fine-mesh cell next to a mesh interface are computed with WENO. The coarse cell fluxes next to the mesh interface, other than the cell face shared with the fine cells, are left to TCD. Other closures involving specialized interpolation formulas for two- and three-dimensional SAMR grids have been derived recently [39,40]. These formulas can be proven to be stable in the linear case and they contribute, as in our interface treatment, to some small amount of numerical dissipation.

For physical discontinuities, the formulation of robust switching criteria for general flow problems remains an open research area. In this paper, we focus on flows for which we can estimate adequately where to use each scheme from the physics and geometry of our problems. The present hybrid scheme utilizes a pressure and density curvature based discontinuity detection criterion to switch schemes from TCD to WENO around shocks. Cell faces in a tight area around shocks are marked according to the following criteria

$$\mathscr{C}_j = \{(x_{j-1/2}, x_{j+1/2}) \in \mathbf{R} : |\xi^p_j| > c_o\Delta x^2, |\xi^\rho_j| > c_o\Delta x^2, \xi^p_j\xi^\rho_j > 0\}, \tag{28}$$

where

$$\xi^p_j = \frac{\bar{p}_{j+1} - 2\bar{p}_j + \bar{p}_{j-1}}{\bar{p}_{j+1} + 2\bar{p}_j + \bar{p}_{j-1}} \quad \text{and} \quad \xi^\rho_j = \frac{\bar{\rho}_{j+1} - 2\bar{\rho}_j + \bar{\rho}_{j-1}}{\bar{\rho}_{j+1} + 2\bar{\rho}_j + \bar{\rho}_{j-1}}. \tag{29}$$

Then, all cells faces in a neighborhood of size $n$ of those that belong to $\mathscr{C}_j$ are also marked as containing the discontinuity producing the set of cell walls $\mathscr{C}^n_j = \bigcup_{s=-n,n}\mathscr{C}_{j+s}$. A three-dimensional split version of this criteria is used in the simulations. Denoting the WENO fluxes as $\boldsymbol{F}^k_{\text{inv-WENO}}$ and the inviscid fluxes computed from the skew-symmetric form as $\boldsymbol{F}^k_{\text{inv-TCD}}$, the hybrid flux takes the form

$$\boldsymbol{F}^k_{\text{inv}} = \begin{cases} \boldsymbol{F}^k_{\text{inv-WENO}} & \text{in } \mathscr{C}^n, \\ \boldsymbol{F}^k_{\text{inv-TCD}} & \text{in } \overline{\mathscr{C}^n}, \end{cases} \tag{30}$$

where $\overline{\mathscr{C}^n}$ denotes the complement of $\mathscr{C}^n$. Note that because the switch affects the fluxes, not the derivative itself, no smoothness requirements are needed in Eq. (30). The only requirement is that the fluxes are consistent with those of the continuous equations being solved. Moreover, experience with this technique has shown that the best results are obtained when the base-line dispersion relationship of the method is preserved across schemes, as it is the case in our approach, cf. [7]. An example of this technique applied to Riemann's one-dimensional wave breaking problem [41] is given in Fig. 3. An extensive discussion of this test problem and its suitability to asses numerical methods for compressible turbulence simulation is also given in [42]. Fig. 3a highlights the cells in which the shock-capturing WENO method needs to be employed, after the wave breaks to avoid unphysical oscillations from the centered scheme. Fig. 3b shows the spectra of the analytical solution together with those computed with three different stencils still without scheme alteration. Note that at the time, at which Fig. 3b is taken, the solution has not steepened enough to necessarily require a shock-capturing scheme. Fig. 3b clearly illustrates that both standard centered methods predict a faster decay of the spectrum at higher wavenumbers than the second-order TCD scheme. TCD tends to overestimate the wavenumber content over the higher wavenumber region slightly, but remains closest to the analytical spectrum

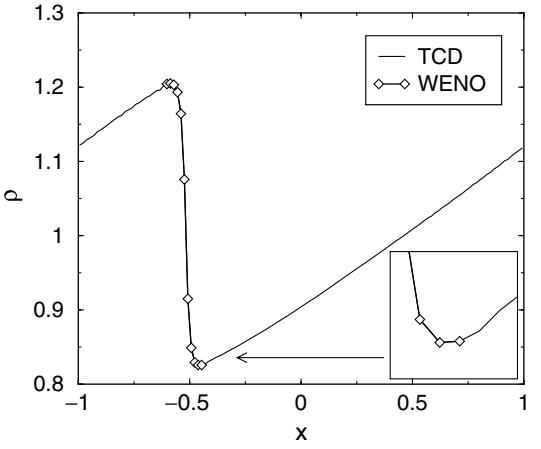


(a) density profile ($2t_s$)

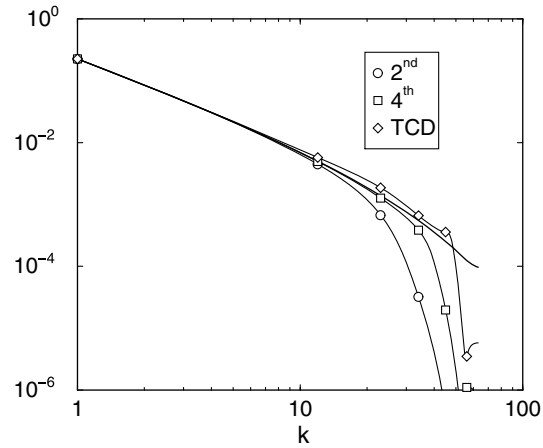


(b) velocity spectra ($t = 0.9t_s$)

Fig. 3. Simple wave solution and spectra of exact and numerical solutions for $\rho_o = 1$, $p_o = 1$, $u_o = 1/4$, $\gamma = 1.4$. (a) density after breaking and (b) spectra of solutions before breaking. The shock first develops at time $t_s = 2/u_o\pi(\gamma + 1)$.

over the widest range. It is this property that makes TCD superior over standard stencils and makes it particular advantageous for turbulence simulations.

### 4.4. Viscous terms

The fluxes of the viscous and diffusion transport terms, $\boldsymbol{f}_{\text{vis}}$, are computed using explicit, centered, second-order 3-point stencils. We avoid the repeated use of the first-order derivative operator in a finite-difference setting (that incidentally leads to wider than necessary stencils and introduces a decoupling at the highest wavenumber) and instead employ edge-based, conservative viscous fluxes. In order to accommodate variable transport coefficients, the viscous transport fluxes are calculated in two steps: The viscous stresses (and diffusive fluxes) are computed at the cell walls using the values between the two adjacent cells and multiplying by the appropriately interpolated value of the transport coefficient. This results in the required viscous transport fluxes. In the second step, these fluxes are added to the total fluxes and the solution is marched in time with Eq. (5). It is straightforward to verify that this method leads directly to a centered 3-point stencil representation of the second-order derivative when the transport coefficients are constant.

## 5. Convergence and numerical dissipation in vortical flows

We report results of two tests that investigate order of accuracy and convergence of the current formulation. We use the vortex solution of the Euler equations employed by [43] to study higher order methods; it is given by the following tangential velocity distribution as a function of the scaled radial coordinate $\eta = r/r_{\text{o}}$

$$u_\theta = u_{\text{o}}\eta\exp(-\eta^2), \tag{31}$$

and

$$p = p_{\text{o}}\left(1 - \frac{\gamma-1}{\gamma}\frac{\rho_{\text{o}}u_{\text{o}}^2}{4p_{\text{o}}}\exp(-2\eta^2)\right)^{\frac{\gamma}{\gamma-1}}, \tag{32}$$

where $r_{\text{o}}$ is the vortex radius and $p/\rho^\gamma = p_{\text{o}}/\rho_{\text{o}}^\gamma$. For the tests presented here we use the dimensionless values $u_{\text{o}} = \pi/4$, $\rho_{\text{o}} = 1$, $p_{\text{o}} = 2$ and $r_{\text{o}} = 0.25$.

Fig. 4 shows the behavior of the $L_1$-norm of the density error for a single vortex calculated using periodic boundary conditions in a rectangular domain $0 < x,y < L = 2.0$ and discretized in each direction with $N$ points. The case $N = 20$ is barely resolved with 4 points across the vortex core. Time integration was performed at a constant, acoustic based, CFL number of 0.9 up to the final time $t_{\text{f}} = 1$; we observed negligible impact on the error using lower CFL numbers. Additionally, we verified that mass, momentum and energy

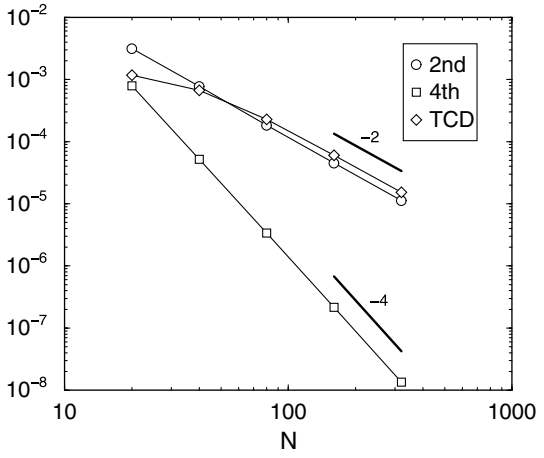


Fig. 4. Convergence error as a function of resolution ($L_1$ norm of the density error). $N = L/\Delta x$ ranges from 20 to 320.

was conserved up to machine precision in all cases. As can be seen in the figure, the advertised order of accuracy is recovered for all choices of $\alpha$, with the 4th-order scheme producing the smallest absolute error. Note that there is no sizable advantage in using the TCD scheme ($\alpha = -0.197$) over the standard second-order scheme in these two-dimensional problems unless the flow structure is not correctly resolved by the 3-point stencil, as shown for $N = 20$ where the TCD error is comparable with that of the 4th-order scheme. This advantage of schemes with 5-point stencils is desirable in three-dimensional LES simulations in which under-resolution is persistent.

To evaluate the effect of our coarse-fine mesh interface closure on numerical dissipation, we extend the previous example by doubling the horizontal extent of the domain to $2L$ and discretize the domain using two resolutions: the central region $L/2 < x < 3L/2$ is refined by a factor of $r = 2$ producing twice the resolution of the remainder of the domain. We also add a second vortex and a constant uniform convective velocity $u_c$ that advects these vorticies through the coarse-fine mesh interfaces. Periodic boundary conditions are used on all boundaries and the vortex parameters are identical to those of the previous test case. The vortices are equally spaced with horizontal separation $L$ and they are initially located with the first vortex a distance $x_o$ from the left boundary $x = 0$.

We investigate three cases, denoted I, II and III, chosen to be representative of the situations that could be encountered in practice when using SAMR for LES. They include: I the common scenario in which vortical cores do not intersect mesh boundaries ($x_o, u_c = 0$), II the case of vortices sitting on the mesh boundaries ($x_o = L/2, u_c = 0$) and III, the worst possible case, of fine-coarse-fine mesh boundary traversal ($x_o = 0$, $u_c = 2L/t_f$). An additional case, IIIb, with the same parameters as III is performed using synchronous (uniform) time integration to estimate the effect on the solution of the computationally more efficient standard time adaptation used in the other three cases, cf. Section 2. We always try to avoid scenarios where Cases II and III arise in our simulations for the reasons that will be discussed next. Only the TCD stencil is used in these tests since the results are of direct relevance to the LES.

Fig. 5 shows the behavior of the $L_1$ norm of the density error as a function of the coarse mesh resolution in all cases. It is observed that the error is quite insensitive to whether the vortices are sitting at the mesh interface or traveling through it; the magnitude of the error is larger in the latter case owing to the larger magnitude of the convective velocity. The convergence rate is second-order for Cases I, II, IIIb and slightly lower for Case III. Use of synchronous time integration does contribute to a slight reduction of the error observed in Case III, as shown in Case IIIb. Finally, Fig. 6 shows the evolution of the averaged kinetic energy variation in the flow for Case III at differing resolutions; although not shown here, better behavior is observed for Case I and II and similar behavior for Case IIIb. It can be seen from the case shown that conservation of kinetic energy improves as the resolution increases, being worst for the unresolved case $N = 20$. Moreover, for a fixed resolution that resolves the flow structure, the variations of kinetic energy are very small.

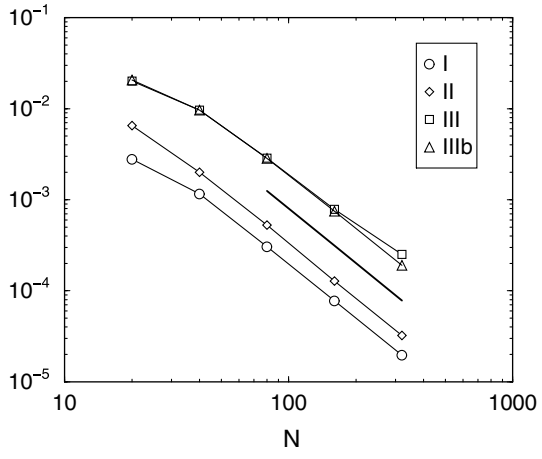


Fig. 5. Convergence of the density error as a function of coarse mesh resolution ($L_1$ norm) for the two vortex periodic system in four different scenarios. Thick line denotes second-order rate. $N = L/\Delta x$ ranges from 20 to 320.

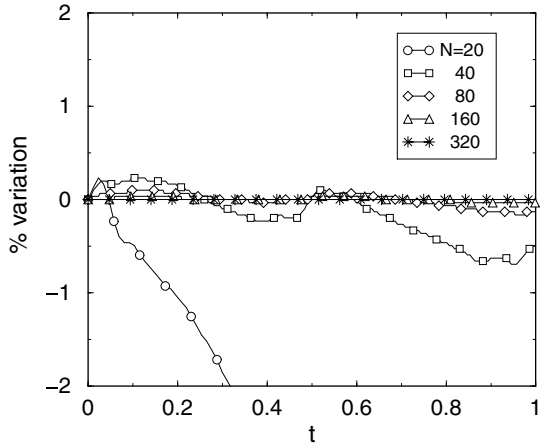


Fig. 6. Percentage variation of kinetic energy for Case III as a function of resolution, where $N = L/\Delta x$ (coarse).

## 6. Three-dimensional LES

In this section, we perform studies of fully turbulent flows with and without shocks both as code validation and to demonstrate the value of using LES with SAMR. The examples chosen here are canonical flows that have been well documented in the experimental literature and the full LES equations, including $\boldsymbol{f}_{\text{visc}}$ and $\boldsymbol{f}_{\text{sgs}}$, are used in the simulations. In the first example, turbulent mixing is induced by a strong shock wave. The moderate runtime of this configuration allow resolution and mesh adaptation studies that demonstrate the savings that can be obtained by our approach over unigrid LES calculations. The second example is a configuration that would be prohibitively expensive on a uniform mesh and has only been enabled by the use of SAMR.

The parallel SAMR system that we employ for these computations is the freely available framework AMROC (Adaptive Mesh Refinement in Object-oriented C++). The adaptive method has been realized completely decoupled from a particular scheme and has been validated extensively on a large number of hydrodynamic test cases [58]. The extensions according to Section 2.3 are implemented effectively in C++ by class inheritance. A key feature of the framework is the efficient parallelization of the entire SAMR algorithm including the flux correction operation on distributed memory machines following a rigorous domain decomposition approach, see [59] for details. During the course of a simulation, the distribution of the evolving SAMR hierarchy to different processors is adjusted dynamically to balance the work and all parallel data structures are automatically rearranged.

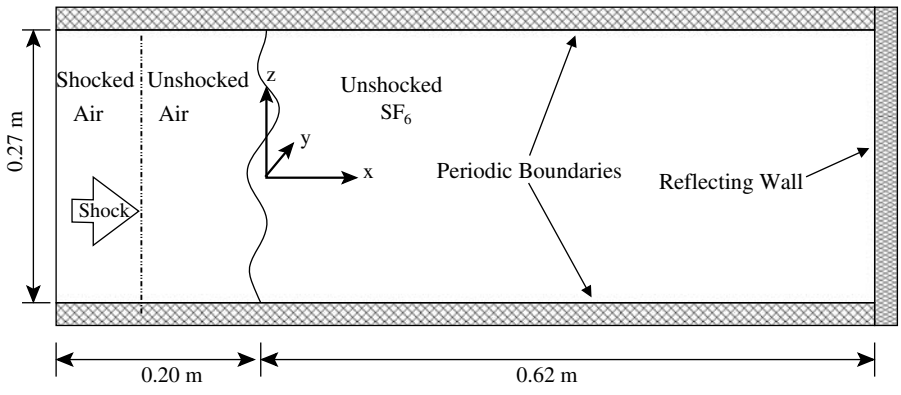


Fig. 7. Sketch of flow geometry.

### 6.1. RM instability with reshock

The first configuration we study is a Richtmyer–Meshkov instability in which an initially planar shock wave interacts with a thin perturbed interface between two gases. The acceleration-induced mixing of the fluids is started when the shock transitions through the interface and is enhanced when the shock returns after its reflection at the closed end of the tube. This flow exercises both the LES and the shock capturing features of the solver with dynamically adaptive meshes. The results of mixing layer growth rate are compared with the experimental measurements by [44]. We chose the experimental case corresponding to a Mach 1.5 shock interacting with an Air–$SF_6$ interface depicted in Fig. 7. The unshocked air has a density of 0.27885 kg/m$^3$ and pressure of 23 kPa. Temperature is uniform in the unshocked side. The domain dimensions are $-0.20\text{ m} \leqslant x \leqslant 0.62\text{ m}$ by $-0.135\text{ m} \leqslant y \leqslant 0.135\text{ m}$ by $-0.135\text{ m} \leqslant z \leqslant 0.135\text{ m}$. Initially, a shock is located at $x = -0.05$ m and travels from left to right, towards the Air–$SF_6$ interface located at $x = 0$ m. A perfectly reflecting boundary condition is used at $x = 0.62$ m and a non-reflective boundary condition is used at $x = -0.2$ m. The time-dependent reference states are shown schematically in the wave diagram of Fig. 8 with the state variables listed in Table 2. These states were determined approximately in an iterative manner from one-dimensional simulations. The lateral walls are modeled using periodic boundary conditions. The initial interface was regularized with a hyperbolic tangent profile of thickness 1 cm. A sinusoidal perturbation was superimposed on this profile with period

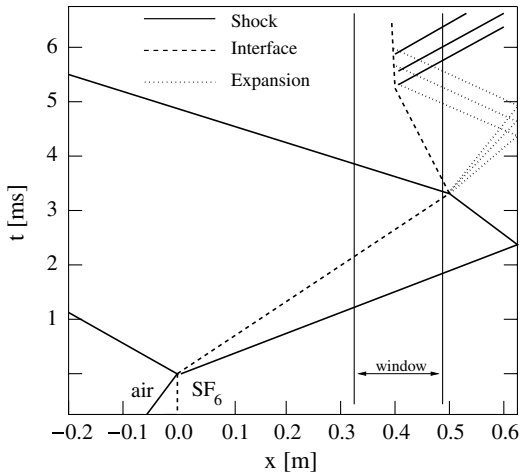


Fig. 8. Shocktube wave interaction diagram. In this diagram, the initial shock comes from the left-hand side and the end wall is located at the far right.

Table 2
Inflow plane boundary condition reference states (bc states) in the different periods of time

| Period (ms) | $\rho_{bc}$ (kg/m$^3$) | $u_{bc}$ (m/s) | $p_{bc}$ (kPa) |
|---|---|---|---|
| $t < 1.05$ | 0.5185 | 235.93 | 56.577 |
| $1.05 \leqslant t < 5.5$ | 0.6330 | 155.45 | 75.055 |
| $5.5 \leqslant t$ | 0.9050 | 0.0 | 125.40 |

Table 3
Computational parameters of the Richtmyer–Meshkov LES simulations

| Case | # Levels | Finest $\Delta x$ (mm) | # Proc. | CPU time (h) |
|---|---|---|---|---|
| A0 | 1 | 4.2 | 16 | – |
| A1 | 2 | 2.1 | 16 | – |
| A2 | 3 | 1.05 | 80 | 11,262 |
| A00 | 1 | 1.05 | 256 | 38,400 |

To avoid confusion, we do not report the timings of A0 and A1 since they were very small runs on a local cluster.

4 cm and amplitude 2.5 mm. The domain was discretized with $196 \times 64 \times 64$ cells on the base grid. Three simulations were carried out as described in Table 3. The refinement ratio between levels was equal to 2 for all levels and directions and the subgrid cutoff scale is set to that of the finest mesh in the simulation. The shock is always captured at the finest resolution available using the detection criterion Eq. (28), but the interface is only well resolved in simulations A1 and A2. The shock detection criteria used the values of $c_o = 2.5 \times 10^3$ and $n = 3$ that proved to give the best results for this problem.

*6.1.1. Physical results*

Fig. 9 shows the evolution of the thickness of the interface with time for the three simulations. There are two important interactions shown in this figure. First, the initial shock reaches the interface close to $t = 0$, compressing it very quickly, while the transmitted shock continues towards the wall. The misalignment of density and pressure gradients deposits vorticity at the interface and initiates the formation of the well-known bubbles and spikes characteristic of acceleration-driven interfaces. This contributes primarily to increased stirring of the flow since there are no sufficiently large gradients to trigger molecular mixing at this time. Second, when the shock is reflected back from the wall, it reshocks the interface at around 3.2 ms after the initial shock interaction. Quickly thereafter, the additional vorticity deposition initiates a more vigorous non-linear phase that leads to mixing until all the kinetic energy is exhausted and a slow growth period of the thickness of the layer is reached beyond 6 ms. Note that, owing to molecular diffusion, mixing will proceed but with a characteristic time scale much larger than that produced by the vorticity deposition during the shock-interface interactions. Fig. 9 also compares the experimentally measured growth rates (thick lines) with the mixing layer thickness obtained from the simulation at the same time periods of the experiment. We observe that the resolution of simulation A0 is insufficient to capture both the initial and post-reshock growth periods. This is largely a consequence of lack of resolution in capturing the initial interface shape, as can be seen in Fig. 9. In simulation A1, the resolution is now sufficient to capture the initial growth period but it fails to capture the post-reshock growth period. Simulation A2 has sufficient resolution to capture both the initial and post-reshock growth periods.

Finally, Fig. 10 shows iso-surfaces of the conserved scalar used to mark the interface, separating air from $SF_6$, at 5 ms for simulation A2. Each of the three iso-surfaces denote the 25%, 50% and 75% $SF_6$ mass fraction iso-surfaces with different intensity of gray (darker denoting $SF_6$ side). The figure also shows the corresponding mesh distribution at this time. It is possible to identify the thinner shock (near $x = 0$ m) leaving the domain and the larger mixing zone to the left.

*6.1.2. Computational costs*

The small simulations A0 and A1 were performed at a local Opteron high-performance cluster while simulations A2 and A00 were performed on QSC, an unclassified Tru64 supercomputer at the Los Alamos National Laboratory; each processor is an Alpha EV6 with 4 GB of memory and a clock speed of

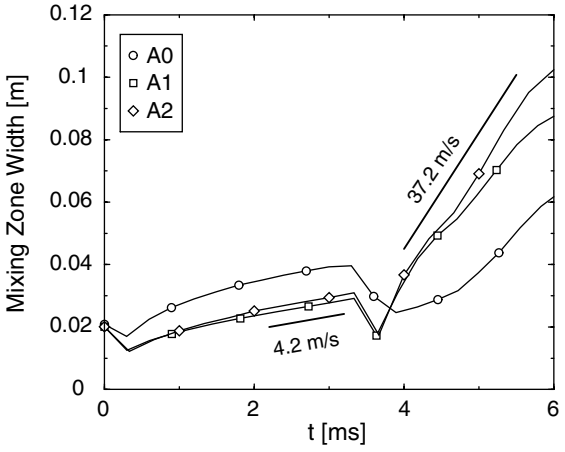


Fig. 9. Evolution of the mixing layer thickness with time for three different resolution LES and experimentally measured growth rates (in the corresponding intervals).

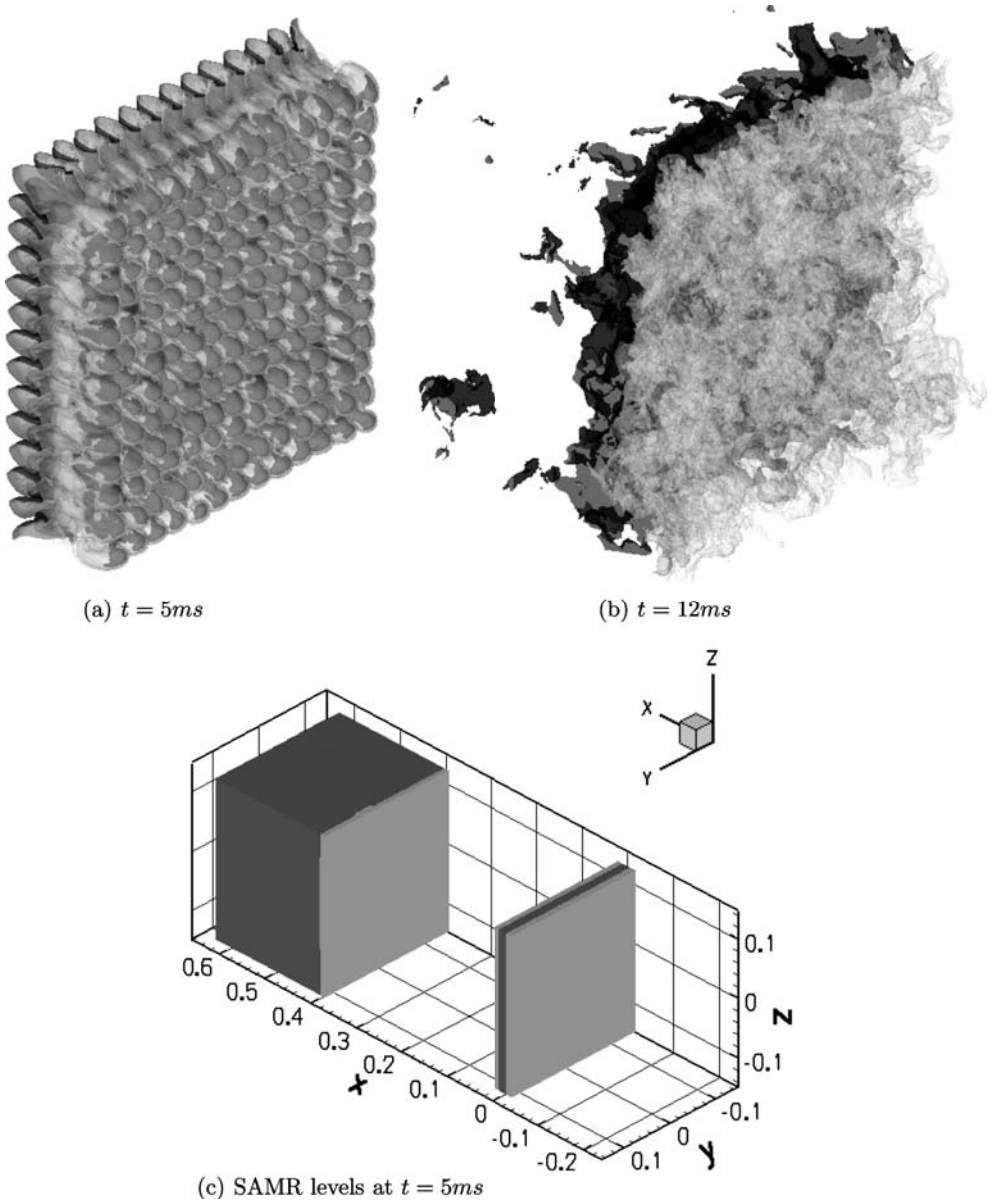


Fig. 10. Composite view of iso-surfaces 0.25, 0.5 and 0.75 of $SF_6$ mass fraction (a) and (b) with levels of refinement (c) of the mesh as light gray (level 1) and dark gray (level 2).

1.25 GHz. Simulation A00, at the same fine resolution of A2, was not run with the SAMR driver but with a simpler Fortran90 driver [45]. Timings and other parameters are reported in Table 3. This provides real comparisons of the actual costs of a simulation with SAMR, including the overhead costs of the mesh hierarchy. From a physical point of view, the mixing width evolution from this unigrid simulation is indistinguishable from that predicted by simulation A2. Nevertheless, the computational cost and storage requirements are not the same. The total grid cell usage as a function of time for A2 is shown in Fig. 11. It can be observed that the cell count varies from a minimum of approximately 4 million cells to a peak of around 14 million. These values can be compared with those of the unigrid simulation, that uses approximately 4 times more storage and took more than 3 times longer to complete. Table 4 shows a detailed cost division of the different parts of the SAMR algorithm. Since the mesh is time evolving we have chosen to present percentage costs at three different times, representative of the physical stages of the simulation. At all times the numerical update within

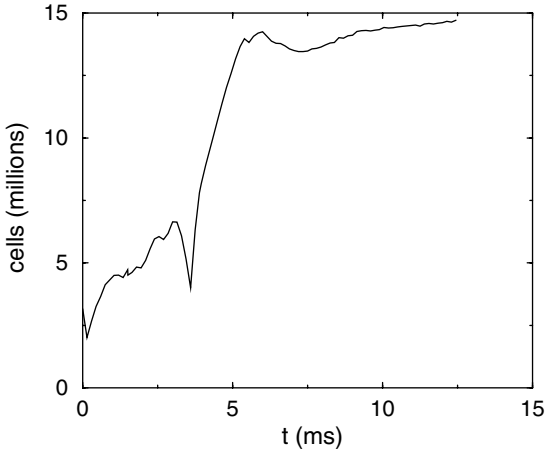


Fig. 11. Evolution of cell count with time.

Table 4
Timings of the SAMR algorithm at different instants of the simulation (rounded to closest integer percentage value)

| Load division at time | 2 ms (%) | 5 ms (%) | 10 ms (%) |
|---|---|---|---|
| Integration | 45 | 66 | 51 |
| Flux correction | 6 | 3 | 4 |
| Boundary synchronization | 45 | 28 | 42 |
| Regridding | 0 | 0 | 0 |
| Partition | 1 | 1 | 1 |
| Recomposition | 1 | 1 | 1 |
| Misc | 1 | 1 | 1 |

the WENO-TCD scheme is the largest portion despite the fact that the computationally very efficient TCD method is used in the vast majority of the domain and the more cumbersome WENO scheme is used only in the direct vicinity of the shock. The second largest portion is the ghost cell synchronization of SAMR subgrids, which is due to the involved parallel communication operations. We emphasize that the usage of multistage Runge–Kutta methods for the temporal advancement necessarily requires a spatial synchronization in every substage, which makes these schemes significantly more communication-intensive than single-step finite volume methods. A relatively small fraction of the cost is also associated with the overhead for the flux correction operation at coarse-fine interfaces. Regridding and (parallel) recomposition are minor, because this application uses only a shallow SAMR hierarchy with few, but relatively large subgrids, which is typical for the LES reported in this paper.

### 6.2. Planar low-speed turbulent jet

We perform large-eddy simulation of the planar turbulent low Mach number jet of [46]. This flow is inhomogeneous with large Reynolds number and involves a wide range of temporal and spatial length-scales. Numerical simulations of this flow in an experiment-size domain with uniform grids would suffer from the resolution requirements of the thin shear layers issuing from the slot and the slender nature of free turbulent jets. While we do not use the top-hat inflow velocity profile reported in [46], adaptive refinement is effectively used to resolve a parabolic inflow velocity profile with the same momentum of said shear layers. The resolution requirement is nevertheless more stringent in the near-flow region than that of the turbulent flow downstream.

The geometry of the flow and the grid cells of the mesh hierarchy in the near-flow region are shown in Fig. 12. The jet Reynolds number of the flow is 30,000 with an exit velocity of 35 m/s and a slot width

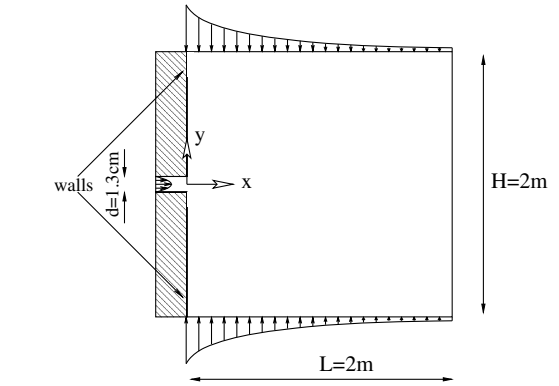


(a) diagram of domain geometry

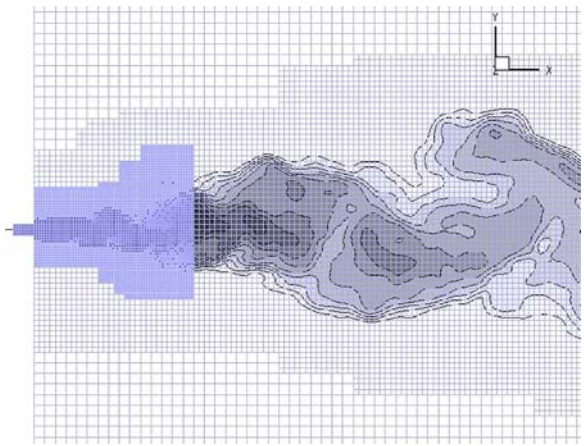

(b) refinement about inflow

Fig. 12. Sketch of domain geometry for jet simulation (a) and zoom of the mesh refinement around the inflow region at one instant in time (b); background iso-levels of conserved scalar shown in (b).

$d = 1.3$ cm. The domain extends with length $L = 2$ m downstream, height $H = 2$ m in the transverse direction and width $W = 50$ cm in the spanwise direction. The LES is performed in a domain of the same size. Characteristic based inflow/outflow conditions are specified in the simulation. The slot inflow is modeled as the superposition of a mean streamwise velocity plus incompressible three-dimensional harmonic velocity fluctuations of magnitude 0.2% at the wavelength of 10 cm. The mean parabolic velocity profile is resolved in the finest mesh of the simulation. The top and bottom boundary velocities have to be specified owing to the entrainment condition.

The domain is discretized using a base grid of $160 \times 160 \times 40$ cells and two additional levels with the refinement ratio 2 for the first level and 4 for the second level. Owing to the geometry of the flow, finest grids are only needed in the first 10% of the domain, where the thin shear layers are present. The next coarsest level of refinement is restricted to the fist half of the domain since it is this region where the turbulence is strongest. The second half of the domain downstream is discretized using the base grid only. For consistency, the subgrid cutoff scale of the turbulence model varies linearly from the fine mesh spacing $\Delta x_f$ at the inflow plane to the coarse mesh size $\Delta x_c$ at the center of the domain, $\Delta_c(x) = \Delta x_f + (\Delta x_c - \Delta x_f)10x/L$.

*6.2.1. Physical results*

Fig. 13 shows iso-contours and iso-surfaces of mixture fraction at one instant in time. We observe all the features characteristic of planar jets, including the flapping generated by the strong vortices resulting from the

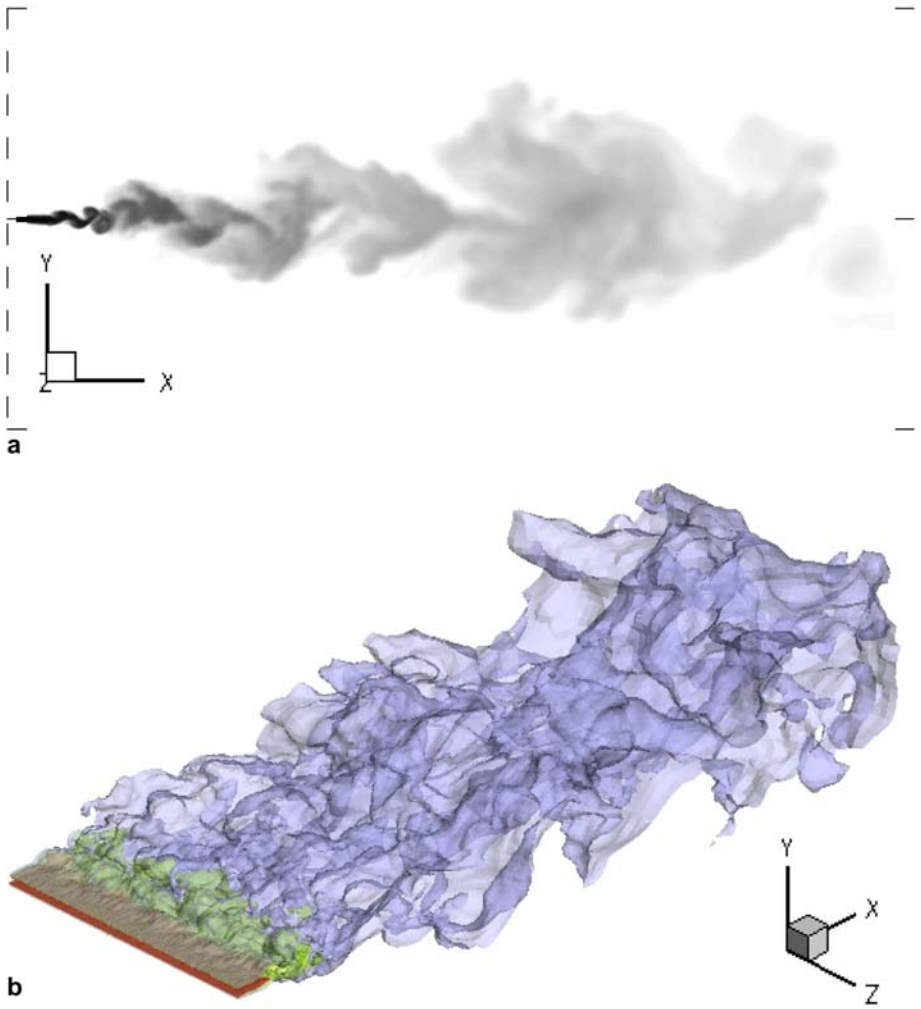


Fig. 13. Side view of iso-contours of mixture fraction (a) and iso-surfaces of mixture fraction and (b) at levels of 0.2, 0.5 and 0.8, respectively.

shear layers interaction. These qualitative results are consistent with experimental observation and DNS data of [47] in smaller domains. Fig. 14 shows comparisons of jet statistics with the experimental measurements of [46]. Fig. 14a compares compensated mean centerline velocity decay, $U_j^2/U_c^2(x)$ with the experimental correlation. For a planar jet, the expected dependence of $U_c(x) \sim x^{-\frac{1}{2}}$ is better measured as the compensated velocity ratio. The agreement between experiment and simulation is satisfactory. Fig. 14b shows normalized turbulence kinetic energy at the centerline as a function of distance. It is observed that the agreement is very good except in the near-flow region where the difference between our inflow velocity profile and those of the experiment have an important effect, $x \leqslant 40d$. Fig. 14c, d show mean velocity profiles and kinetic energy at different stations downstream of the inflow plane also with good self-similar collapse as expected.

*6.2.2. Computational costs*

In this simulation, we utilize up to $4 \times 10^6$ grid cells, including all levels. The savings compared to an equivalent unigrid mesh are a factor of about 130 in storage and runtime. This case exemplifies the enormous cost reductions that can be obtained by applying SAMR to LES in which typical simulations often have to be run for $\mathcal{O}(10^5 - 10^6)$ time steps to obtain converged statistical data.

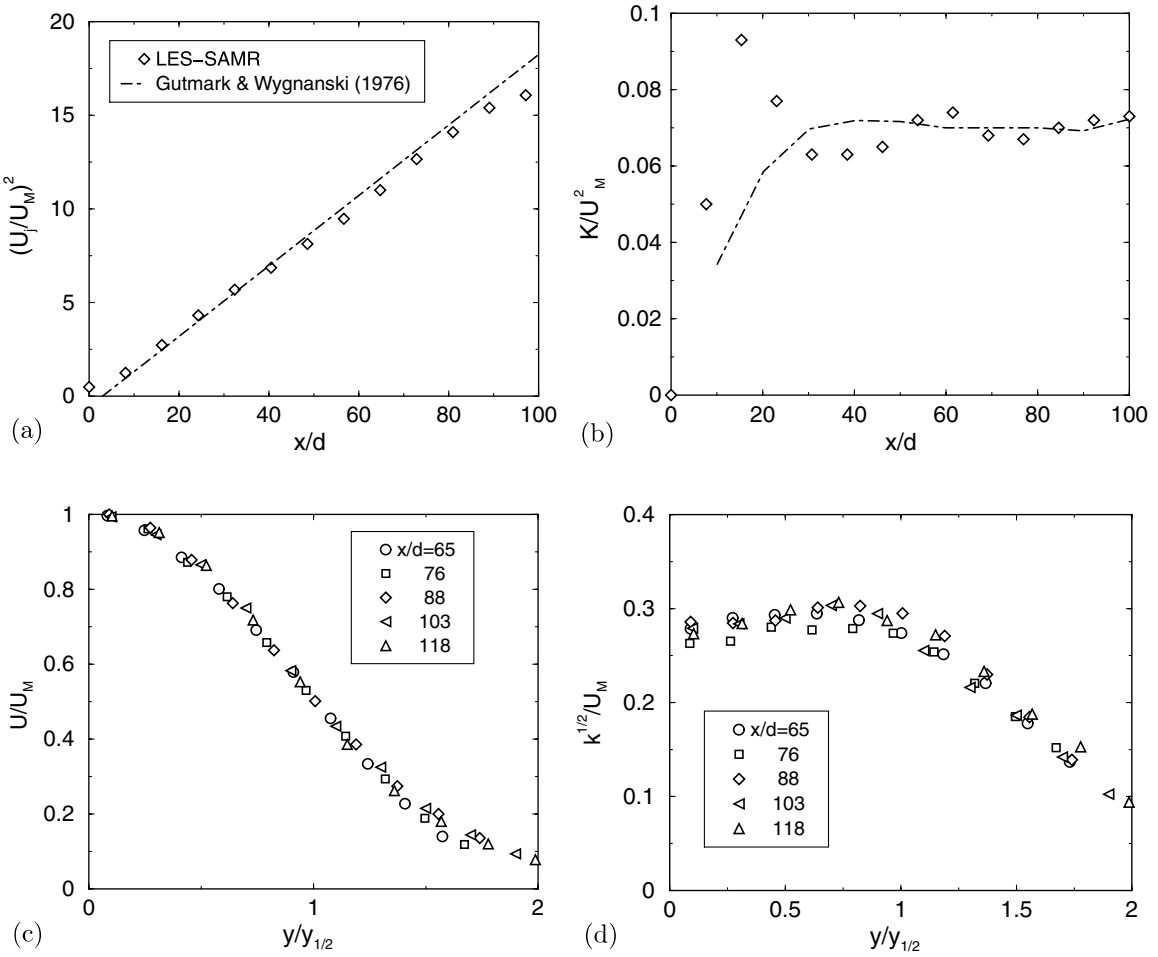


Fig. 14. Comparison with experiments: (a) centerline averaged velocity decay, (b) normalized centerline turbulence kinetic energy, (c) self-similar streamwise velocity at different planes and (d) self-similar normalized kinetic energy at different planes.

## 7. Conclusions

We have described an extension of the classical SAMR algorithm, after Berger and Colella, to meet the requirements of large-eddy simulation. We have also constructed a hybrid solver whose formulation uses low-numerical-dissipation, centered schemes in skew-symmetric form within patches of uniform resolution in turbulent regions of the flow, and upwinding in regions where shocks exists and at fine-coarse mesh interfaces. The upwinding operator is based on a modified version of the WENO method that matches reference stencils to the centered scheme. This is crucial in order to minimize spurious reflections arising when the scheme transitions from centered to upwind form. A conservative formulation in flux form is used to ensure weak convergence. A positivity preserving third-order Runge–Kutta time integration solver is adapted to the SAMR methodology to ensure conservation at mesh interfaces.

Several example LES simulations have been analyzed. We discussed the order of accuracy and minimal LES-SAMR refinement conditions and, in particular, the problem of energy generation/loss at fine-coarse mesh interfaces of our overall method. In this respect, it is observed that our fine-coarse mesh interface treatment performs very well with respect to convergence and conservation of kinetic energy as long as the flow structures passing through the mesh interface are reasonably well resolved. From the validation point of view, the present LES-SAMR method allowed us to compare simulation results obtained on conventional distributed memory systems of moderate size directly to the shock-induced mixing flow produced by the Richtmyer–

Meshkov instability and to three-dimensional turbulent jet statistics. The good agreement between simulations and experimental data confirms the relevancy of the approach described. Moreover, substantial savings generated by the SAMR approach allow the simulation of flows that would have prohibitively large memory and computational requirements if unigrid methods were used.

**Acknowledgments**

This work was supported by the ASC program of the Department of Energy under subcontract No. B341492 of DOE Contract W-7405-ENG-48.

## Appendix A. Boundary closure

The boundary closure used to discretize the governing equations is derived using the energy approach of [48,49]. This method constructs a biased numerical discretization of the first-order derivative at the boundary of the domain for the linear equation

$$\frac{\mathrm{d}w}{\mathrm{d}t} + \lambda \frac{\mathrm{d}w}{\mathrm{d}x} = 0, \tag{A.1}$$

that satisfies the summation by parts property. This technique produces boundary closures that are stable and robust in practice. Briefly, it requires that the discretization of the first-order derivative takes the form

$$\mathscr{H}\frac{\mathrm{d}w}{\mathrm{d}x} = \frac{1}{\Delta x}\mathscr{D}w, \tag{A.2}$$

where $w$ is the equally spaced discretized solution vector $w_j = w(j\Delta x, t)$ with $j = 0,1,2,\ldots$ and we consider for simplicity the semi-infinite case since the interior stencil is explicit. For $j > 1$, matching with the TCD stencil, Eq. (18), is imposed; i.e., away from the boundary. The matrix $\mathscr{H}$ is symmetric and positive definite and in our case will be taken as the diagonal matrix $\mathscr{H} = \mathrm{diag}\{h_1, h_2, 1, 1, \ldots\}$ for stability reasons [48]. The matrix $\mathscr{D}$ is almost anti-symmetric with the only non-zero term in the diagonal being the corner term, that equals $d_{1,1} = -1/2$. The boundary closure that results is given by

$$\Delta x h_1 \frac{\mathrm{d}w_1}{\mathrm{d}x} = -\frac{1}{2}w_1 + d_{1,2}w_2 + \alpha w_3, \tag{A.3}$$

$$\Delta x h_2 \frac{\mathrm{d}w_2}{\mathrm{d}x} = -\mathrm{d}_{1,2}w_1 + \beta w_3 + \alpha w_4, \tag{A.4}$$

where $\alpha$ is the parameter in our stencil. The coefficients, $h_1$, $h_2$ and $d_{1,2}$, are obtained by matching terms in Taylor series expansions in powers of $\Delta x$ to first-order of accuracy, giving

$$d_{1,2} = \frac{1}{2} - \alpha \quad h_1 = \frac{1}{2} + \alpha \quad h_2 = 1 - \alpha, \tag{A.5}$$

and according to [50] we retain second-order global accuracy. It can be verified that $h_1, h_2 > 0$ for all the values of $\alpha$ of interest in this study so that $\mathscr{H}$ is positive definite. This method is energy stable and also verifies GKS [51,52] and asymptotic stability.

Numerically, Dirichlet boundary conditions are imposed using the simultaneous approximation term (SAT) penalty approach of [49]. This is achieved by altering the governing equations at the boundary, in our case at $x = 0$ when $\lambda > 0$, such that there we solve

$$\frac{\mathrm{d}w}{\mathrm{d}t} + \frac{\lambda}{\Delta x}\mathscr{H}^{-1}(\mathscr{D}w - \tau d_{1,1}\mathscr{S}(w_0 - w_{\mathrm{bc}}(t))) = 0, \tag{A.6}$$

where the theoretical framework of [49] and [53] shows that for the diagonal form of $\mathscr{H}$, the vector $\mathscr{S} = \{1, 0, 0, \ldots\}^{\mathrm{T}}$ with $\tau \geqslant 1$ and $w_{\mathrm{bc}}(t)$ is the incoming wave strength. Typically, a value of $1.5 < \tau < 2$ was used in the simulations discussed in this paper.

The cases of interest in this paper correspond to flows at high Reynolds numbers where the governing equations form a system of almost hyperbolic equations. We neglect in this discussion the contribution of subgrid

fluxes and transport (viscous, heat conduction and diffusion) so that $\boldsymbol{f}^k = \boldsymbol{f}^k_{\text{inv}}$ within this section and consider the leading order effect of waves traveling normal to a boundary. We use characteristic based boundary conditions [54] at open boundaries formulated in terms of the discrete methods detailed previously. This enables long time integration of the governing equations. We introduce the eigensystem of the linearized equations and the characteristic vector, $\boldsymbol{w}$, related to the conservative vector of state, $\boldsymbol{q}$, through

$$\partial \boldsymbol{w} = \mathscr{R}^{-1} \partial \boldsymbol{q}, \tag{A.7}$$

where $\mathscr{R}$ is the right-eigenvector matrix of the Jacobian of the flux vector normal to the boundary,

$$\mathscr{A} = \frac{\partial \boldsymbol{f}}{\partial \boldsymbol{q}}. \tag{A.8}$$

The diagonalized system becomes

$$\frac{\partial \boldsymbol{w}}{\partial t} + \Lambda \frac{\partial \boldsymbol{w}}{\partial x} = 0, \tag{A.9}$$

where the matrix $\Lambda$ is diagonal, $\Lambda = \text{diag}\{\lambda_1, \lambda_2, \ldots, \lambda_{N+5}\}$, and the entries $\lambda_m$ are the eigenvalues of the hyperbolic system ordered in increasing magnitude, $\lambda_1 = u - c$, $\lambda_{2-(N+4)} = u$ and $\lambda_{N+5} = u + c$, where $u$ is the flow velocity normal to the boundary and $c$ is the speed of sound. Eq. (A.6) is then multiplied by $\mathscr{R}$ to obtain the corresponding primitive equations with SAT correction for those characteristic directions with incoming $\lambda_i$. Finally, subsonic outflows use the approximate method developed by [55] and viscous terms are handled following [56].

## Appendix B. Subgrid model

The quantities that need to be modeled are subgrid momentum stresses

$$\tau_{ik} = \bar{\rho}(\widetilde{u_i u_k} - \tilde{u}_i \tilde{u}_k) - (\bar{\sigma}_{ik} - \tilde{\sigma}_{ik}), \tag{B.1}$$

the subgrid total energy transfer

$$\sigma^e_k = \bar{\rho}(\widetilde{h u_k} - \tilde{h}\tilde{u}_k) + \frac{\bar{\rho}}{2}(\widetilde{u_j u_j u_k} - \widetilde{u_j u_j}\tilde{u}_k) - (\overline{\sigma_{kj} u_j} - \tilde{\tau}_{kj}\tilde{u}_j) + (\bar{q}_k - \tilde{q}_k), \tag{B.2}$$

and the subgrid scalar transport

$$\sigma^l_k = \bar{\rho}(\widetilde{Y_l u_k} - \widetilde{Y}_l \tilde{u}_k) + (\bar{J}^l_k - \tilde{J}^l_k). \tag{B.3}$$

The last term appearing in Eqs. (B.1) and (B.3) and the last two terms in Eq. (B.2) will be neglected here because they contribute typically very little to the total budgets for large Reynolds number flows.

The stretched-vortex model after [30–32] is used for the turbulent transport terms. In this model, it is assumed that subgrid motion is produced by subgrid vortical structures. The subgrid terms can then be expressed as

$$\tau_{ik} = \bar{\rho} k_{\text{sgs}}(\delta_{ik} - e_i e_k), \tag{B.4}$$

$$\sigma^e_k = \frac{1}{2}\bar{\rho}\Delta_c k^{1/2}_{\text{sgs}}(\delta_{jk} - e_j e_k)\frac{\partial \tilde{h}}{\partial x_j}, \tag{B.5}$$

and

$$\sigma^l_k = \frac{1}{2}\bar{\rho}\Delta_c k^{1/2}_{\text{sgs}}(\delta_{jk} - e_j e_k)\frac{\partial \widetilde{Y}_l}{\partial x_j}, \tag{B.6}$$

where $e_i$ are the direction cosines of the subgrid vortex axis and $\Delta_c$ is the subgrid cutoff length scale. The subgrid kinetic energy $k_{\text{sgs}}$ is given by

$$k_{\text{sgs}} = \int_{k_c}^{\infty} E(k)\mathrm{d}k, \tag{B.7}$$

where $k_c = \pi/\Delta_c$. The subgrid vortices are assumed to take the form of a Lundgren stretched-spiral vortex with shell-summed subgrid energy spectrum of the form

$$E(k) = \kappa_o \epsilon^{2/3} k^{-5/3} \exp(-2k^2 v/(3|a|)). \tag{B.8}$$

The parameter $\kappa_o$ is the Kolmogorov pre-factor, $\epsilon$ is the local cell-averaged dissipation and $a = \tilde{S}_{ij} e_i^v e_j^v$ is the axial strain along the subgrid vortex axis provided by the locally resolved flow with rate-of-strain tensor

$$\tilde{S}_{ij} = \frac{1}{2}\left(\frac{\partial \tilde{u}_i}{\partial x_j} + \frac{\partial \tilde{u}_j}{\partial x_i}\right).$$

In order to implement the model, the $e_i$ must be specified or otherwise determined, and the composite parameter $\kappa_o \epsilon^{2/3}$ calculated. The $e_i$ are modeled by alignment with extensional eigenvectors of $\tilde{S}_{ij}$ and with the resolved-scale vorticity, cf. [32]. The parameter $\kappa_o \epsilon^{2/3}$ is calculated using resolved-scale, second-order velocity structure functions, see [57]. This can take two forms: In the first, a local spherical average is used to estimate the second-order, longitudinal velocity structure function which can then be matched to the model subgrid spectrum. In the second, an average longitudinal structure function on a circle of radius $r$, with origin at the cell center, and lying in a pre-specified plane is computed for each cell. The chosen plane usually contains at least one homogeneous flow direction. If the circular-averaged structure function is $\widetilde{F}_2^c(r;\mathbf{x})$ and it is assumed that $r$ lies in the inertial range, then one can obtain [57]

$$\kappa_o \epsilon^{2/3} = \frac{\pi \widetilde{F}_2^c(r;\mathbf{x})}{2\Delta^{2/3} \int_{\phi=0}^{2\pi} \int_{s=0}^{\pi} s^{-5/3} \left[1 - J_0\left(s \frac{r}{\Delta} \sqrt{1 - \sin^2\psi \cos^2\phi}\right)\right] \mathrm{d}s\, \mathrm{d}\phi}. \tag{B.9}$$

In Eq. (B.9) the cutoff wavenumber is $k_c = \pi/\Delta$ where $\Delta$ is the local cell size, and $\psi$ is the angle between the subgrid vortex axis and the normal to the plane. All other quantities on the right-hand side can be computed from the resolved-scale velocity field. The integral in the denominator is a function of $r/\Delta$ and $\psi$ and can be estimated in approximate analytical form. Typically, $r = \Delta$. In the tensor-diffusivity modeling of subgrid scalar transport equations (B.6) and (B.5), a dimensionless parameter on the right-hand side is taken equal to unity, see [31] and [32]. The stretched-vortex model is entirely local in the sense that no spatial averaging is required to determine model parameters.

## References


[1] M.J. Berger, J. Oliger, Adaptive mesh refinement for hyperbolic partial-differential equations, J. Comp. Phys. 53 (3) (1984) 484–512.
[2] M.J. Berger, P. Colella, Local adaptive mesh refinement for shock hydrodynamics, J. Comp. Phys. 82 (1) (1989) 64–84.
[3] R.F. Warming, R.M. Beam, Upwind 2nd-order difference schemes and applications in aerodynamic flows, AIAA J. 14 (9) (1976) 1241–1249.
[4] C.W. Shu, T.A. Zang, G. Erlebacher, D. Whitaker, S. Osher, High-order ENO schemes applied to 2-dimensional and 3-dimensional compressible flow, Appl. Numer. Math. 9 (1) (1992) 45–71.
[5] X.D. Liu, S. Osher, T. Chan, Weighted essentially non-oscillatory schemes, J. Comp. Phys. 115 (1) (1994) 200–212.
[6] F. Ducros, F. Laporte, T. Souleres, V. Guinot, P. Moinat, B. Caruelle, High-order fluxes for conservative skew-symmetric-like schemes in structured meshes: application to compressible flows, J. Comp. Phys. 161 (1) (2000) 114–139.
[7] D.J. Hill, D.I. Pullin, Hybrid tuned center-difference-WENO method for large eddy simulations in the presence of strong shocks, J. Comp. Phys. 194 (2) (2004) 435–450.
[8] M. Gerritsen, P. Olsson, Designing and efficient solution strategy for fluid flows. ii. Stable high-order central finite difference schemes on composite adaptive grids with sharp shock resolution, J. Comp. Phys. 147 (2) (1998) 293–317.
[9] J. Nordström, M. Carpenter, Boundary and interface conditions for high-order finite-difference methods applied to the Euler and Navier–Stokes equations, J. Comp. Phys. 148 (2) (1999) 621–645.
[10] M. Braack, A. Ern, Coupling multimodelling with local mesh refinement for the numerical computation of laminar flames, Combust. Sci. Technol. 8 (4) (2004) 771–788.
[11] P. Lax, B. Wendroff, Systems of conservation laws, Commun. Pure Appl. Math. 13 (2) (1960) 217–237.
[12] E.F. Toro, Riemann Solvers and Numerical Methods for Fluid Dynamics, Springer, Berlin, 1997.
[13] M. Berger, On conservation at grid interfaces, SIAM J. Numer. Anal. 24 (5) (1987) 967–984.
[14] R.B. Pember, L.H. Howell, J.B. Bell, P. Colella, W.Y. Crutchfield, W.A. Fiveland, J.P. Jessee, An adaptive projection method for unsteady, low-mach number combustion, Combust. Sci. Technol. 140 (1) (1998) 123–168.

[15] L.H. Howell, R.B. Pember, P. Colella, J.P. Jesse, W.A. Fiveland, A conservative adaptive-mesh algorithm for unsteady, combined-mode heat transfer using the discrete ordinates method, Num. Heat Trans. 35 (B) (1999) 407–430.
[16] L.H. Howell, J.A. Greenough, Radiation diffusion for multi-fluid Eulerian hydrodynamics with adaptive mesh refinement, J. Comp. Phys. 184 (1) (2003) 53–78.
[17] S.K. Lele, Compact finite differences schemes with spectral-like resolution, J. Comp. Phys. 103 (1992) 16–42.
[18] W.J. Feiereisen, W.C. Reynolds, J.H, Ferziger, Numerical simulation of a compressible, homogeneous, turbulent shear flow. Technical Report TF-13, Dept. Mech. Engineering, Stanford University, 1981.
[19] T.A. Zang, On the rotation and skew-symmetric forms for incompressible flow simulation, Appl. Numer. Math. 7 (1) (1991) 27–40.
[20] G.A. Blaisdell, Numerical simulation of compressible homogeneous turbulence, PhD thesis, Stanford University, 1991.
[21] A.E. Honein, P. Moin, Higher entropy conservation and numerical stability of compressible turbulence simulations, J. Comp. Phys. 201 (2) (2004) 531–545.
[22] R. Samtaney, D.I. Pullin, B. Kosovic, Direct numerical simulation of decaying compressible turbulence and shocklet statistics, Phys. Fluids 13 (5) (2001) 1415–1430.
[23] S.B. Pope, Ten questions concerning the large-eddy simulation of turbulent flows, New J. Phys. 6 (2004) 35.
[24] L.N. Trefethen, Stability of finite-difference models containing two boundaries or interfaces, Math. Comput. 45 (172) (1985) 279–300.
[25] D.V. Gaitonde, M.R. Visbal, Advances in the application of high-order techniques in simulation of multi-disciplinary phenomena, Int. J. Comput. Fluid Dyn. 17 (2) (2003) 95–106.
[26] C.W. Shu, S. Osher, Efficient implementation of essentially non-oscillatory shock-capturing schemes, J. Comp. Phys. 77 (2) (1988) 439–471.
[27] K.A. Hessenius, M.M. Rai, Applications of a conservative zonal scheme to transient and geometrically complex problems, Comp. Fluids 14 (1) (1986) 43–58.
[28] M.M. Rai, A conservative treatment of zonal boundaries for Euler equation calculations, J. Comp. Phys. 62 (1986) 472–503.
[29] S. Gottlieb, C-W. Shu, E. Tadmor, Strong stability-preserving high-order time discretization methods, SIAM Rev. 43 (1) (2001) 89–112.
[30] A. Misra, D.I. Pullin, A vortex-based subgrid model for large-eddy simulation, Phys. Fluids 9 (8) (1997) 2443–2454.
[31] D.I. Pullin, Vortex-based model for subgrid flux of a passive scalar, Phys. Fluids 12 (9) (2000) 2311–2319.
[32] B. Kosović, D.I. Pullin, R. Samtaney, Subgrid-scale modeling for large-eddy simulations of compressible turbulence, Phys. Fluids 14 (4) (2002) 1511–1522.
[33] G.-S. Jiang, C.-W. Shu, Efficient implementation of weighted ENO schemes, J. Comp. Phys. 126 (1) (1996) 202–228.
[34] R. Vichnevetsky, Wave propagation and reflection in irregular grids for hyperbolic equations, App. Num. Math. 3 (1987) 133–166.
[35] S. Ghosal, An analysis of numerical errors in large-eddy simulations of turbulence, J. Comp. Phys. 125 (1) (1996) 187–206.
[36] A. Benkenida, J. Bohbot, J.C. Jouhaud, Patched grid and adaptive mesh refinement strategies for the calculation of the transport of vortices, Int. J. Numer. Meth. Fluids 40 (2002) 855–873.
[37] Y. Morinishi, T.S. Lund, O.V. Vasilyev, P. Moin, Fully conservative higher order finite difference schemes for incompressible flow, J. Comp. Phys. 143 (1) (1998) 90–124.
[38] B. Cockburn, C.-W. Shu, The local discontinuous Galerkin method for time-dependent convection diffusion systems, SIAM J. Numer. Anal. 35 (1998) 2440.
[39] P. Lötstedt, S. Söderberg, A. Ramage, L. Hemmingsson-Frändén, Implicit solution of hyperbolic equations with space–time adaptivity, BIT 42 (1) (2002) 134–158.
[40] L. Ferm, P. Lötstedt, Accurate and stable grid interfaces for finite volume methods, App. Num. Math 49 (2004) 207–224.
[41] B. Riemann, 1890.
[42] A.W. Cook, W.H. Cabot, A high-wavenumber viscosity for high-resolution numerical methods, J. Comp. Phys. 195 (2) (2004) 594–601.
[43] D.S. Balsara, C.W. Shu, Monotonicity preserving weighted essentially non-oscillatory schemes with increasing high order of accuracy, J. Comp. Phys. 160 (2000) 405–452.
[44] M. Vetter, B. Sturtevant, Experiments on the Richtmyer–Meshkov instability on a air/sf$_6$ interface, Shock Waves 4 (5) (1995) 247–252.
[45] D.J. Hill, C. Pantano, D.I. Pullin, Large-eddy simulation and multiscale modeling of a Richtmyer–Meshkov instability flow with reshock, J. Fluid Mech. 557 (2006) 29–61.
[46] E. Gutmark, I. Wygnanski, The planar turbulent jet, J. Fluid Mech. 73 (3) (1976) 465–495.
[47] S.A. Stanley, S. Sarkar, J.P. Mellado, A study of the flow-field evolution and mixing in a planar turbulent jet using direct numerical simulation, J. Fluid Mech. 450 (2002) 377–407.
[48] B. Strand, Summation by parts for finite difference approximations for d/d$x$, J. Comp. Phys. 110 (1) (1994) 47–67.
[49] M.H. Carpenter, D. Gottlieb, S. Abarbanel, Time-stable boundary conditions for finite difference schemes solving hyperbolic systems: methodology and application to high-order compact schemes, J. Comp. Phys. 111 (1994) 220.
[50] B. Gustafsson, Convergence rate for difference approximations to mixed initial boundary-value problems, Math. Comput. 29 (130) (1975) 396–406.
[51] B. Gustafsson, H.O. Kreiss, A. Sundstrom, Stability theory of difference approximations for mixed initial boundary-value problems ii, Math. Comp. 26 (119) (1972) 649–686.
[52] J.C. Strikwerda, Initial boundary value problems for the method of lines, J. Comp. Phys. 34 (1980) 94–107.
[53] S.S. Abarbanel, A.E. Chertock, Strict stability of high-order compact implicit finite-difference schemes: the role of boundary conditions for hyperbolic PDEs, I., J. Comp. Phys. 160 (2) (2000) 42–66.

[54] Kevin W. Thompson, Time dependent boundary conditions for hyperbolic systems, J. Comp. Phys. 68 (1987) 1–24.
[55] D.H. Rudy, J.C. Strikwerda, A non-reflective outflow boundary conditions for subsonic Navier–Stokes calculations, J. Comp. Phys. 36 (1) (1980) 55–70.
[56] T.J. Poinsot, S.K. Lele, Boundary conditions for direct simulations of compressible viscous flows, J. Comp. Phys. 101 (1992) 104–129.
[57] T. Voelkl, D.I. Pullin, A physical-space version of the stretched-vortex subgrid-stress model for large-eddy simulations, Phys. Fluids 12 (7) (2000) 1810–1825.
[58] R. Deiterding, Parallel adaptive simulation of multi-dimensional detonation structures. PhD thesis, Brandenburgische Technische Universität Cottbus, 2003.
[59] R. Deiterding, Construction and application of an AMR algorithm for distributed memory computers, in: T. Plewa, T. Linde, V.G. Weirs (Eds.), Adaptive Mesh Refinement – Theory and Applications, vol. 41, Lecture Notes in Computational Science and Engineering, Springer, 2005, pp. 361–372.